Supporting information

Engineering Aqueous Electrolytes with Vicinal S-based Organic Additives for Highly Reversible Zinc-Ion Batteries

Teng Li [+], Ahmad Naveed [+], Jiongzhi Zheng [+], Bixian Chen, Mingfeng Jiang, Biyuan Liu, Yu Zhou, Xiaowei Li, Mingru Su, Ruiqiang Guo, Joy Sumner,[*] Cheng Chao Li,[*] and Yunjian Liu[*].

Experimental Portion

The preparation of nano-$NaV_3O_8 \cdot 1.35H_2O$ (NVO) cathode

The synthesis of nano-$NaV_3O_8 \cdot 1.35H_2O$ follows a straightforward method according to a reported work.[1] 0.5 g commercial V_2O_5 powder (purchased from Macklin, 99%) was added to deionized (DI) water with a sonication for 1 h. Then 0.1 M NaCl was slowly added into the obtained solution at a heating temperature of 40 °C in an oil bath for 3 days with a stirring at 500 rpm. The obtained mixture was centrifugated and washed three times with DI water. Finally, the washed slurry was dried at 60 °C under vacuum for 12 h.

To prepare the nano-$NaV_3O_8 \cdot 1.35H_2O$ cathode, the NVO solid, binder (PVDF) and conductive agent (acetylene black) were mixed with a mass ratio of 7:2:1. Then the mixture was ground in a mortar for 35 minutes. Next, N-methyl-2-pyrrolidone (NMP) was added with a proper amount and continuously ground for 20 minutes. The carbon paper was cut to a circular shape (diameter: 11 mm) to act as the current collector for the high conductivity and contact area with the active material for cathodes. After the above, the ground slurry was painted on the carbon paper and dried in a vacuum even at 60 °C.

Electrochemical measurements

The two-electrode coin cells (Zn-Zn symmetrical cells, Zn-Ti/Cu asymmetrical cells and Zn-ZVO full cells) were assembled with CR2025 shells at room temperature in an open atmosphere. The electrolytes for Zn-Zn and Zn-Ti/Cu cells were prepared by employing 2 M $ZnSO_4$ with or without SPS additive with a volume of 80 μL. The electrolytes for full cells have an addition of 0.5 M Na(OTF) to inhabit the desolation of the NVO cathode, based on the electrolytes for Zn-Zn and Zn-Ti/Cu.[2] The circular zinc electrodes used in coin cells were cut on the commercial foil, which has a thickness of 100 μm, with a diameter of 12 mm and polished with grit-1500 abrasive paper to remove the oxide layer on Zn surface. The titanium electrodes (0.01 mm thickness) and copper electrodes (0.01 mm thickness) for Zn-Ti/Cu batteries were also cut with a

diameter of 12 mm. The titanium, copper and polished zinc electrodes were carefully washed with DI water and ethanol to keep the electrodes clean. The Zn-Cu cells were employed to research the reversibility of zinc anode in Coulombic efficiency (CE) tests. Glass fibre (GF/A, 260 μm thickness) was employed as the separator. The cycling performance was tested at Neware battery system at room temperature in a dry open atmosphere. Chronoamperometry (CA, Zn-Zn), linear sweep voltammetry (LSV, Zn-Ti), cyclic voltammetry (CV, full cell), electrochemical impedance spectroscopy (EIS, Zn-Zn) were tested on the CHI660E (Shanghai Chenhua Co., Ltd.)

Characterizations

The microstructure was observed by field emission electron microscope (FEI NovaNano 450, USA) and the composition was analyzed by the X-ray diffractometer (SmartLab, Japan) at a scan rate of 10°/min from 5°-85°. The Raman spectra were tested on Thermo Scientific DXR (USA). Nuclear magnetic resonance (NMR) spectroscopy was conducted by Bruker Ultra Shield Plus (Germany, 400 MHz) to investigate the reconstruction effect of H-bond. Atomic force microscope (AFM) test was observed on Multimode-8-AM (Bruker, USA). X-ray photoelectron spectroscopy (XPS) was tested on Thermo Scientific ESCALAB 250Xi (USA). Grazing incidence wide-angle X-ray scattering was conducted on Xenocs Xeuss 2.0 (France). The ionic conductivity was tested on DDS-307 (Shanghai Rex Instrument, China). The in-situ optical tests were utilized with an optical microscope (Yuescope YD650, China).

Molecular dynamic simulations

Two different models were constructed to compare the de-solvation performance of SPS. In the first model, the electrolyte, with dimensions of 27.695 Å × 31.979 Å × 62.000 Å, was set, containing 2 M $ZnSO_4$ in H_2O. In the second model, 0.2 M SPS-2 M $ZnSO_4$ electrolyte with the same dimensions was built, containing $ZnSO_4$, H_2O and SPS.

After geometry optimization, the liquid structures were subjected to molecular dynamics (MD) simulations under the NVT ensemble (T = 300 K) with a time step of

1 fs and a total simulation time of 5 ns. The distribution of O atoms on the Zn slab surface was recorded every 100 steps, with the distance from 13 Å to 33 Å divided into 200 boxes with a step size of 0.1 Å.

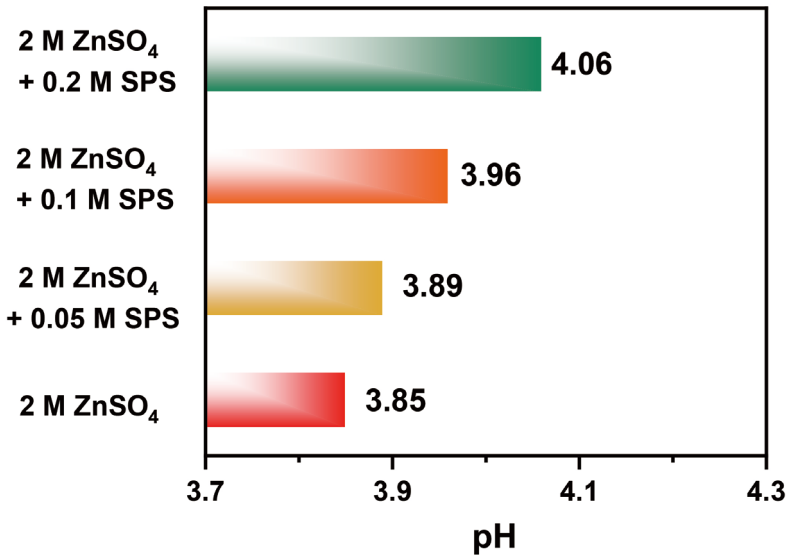


Figure S1. The pH values for $ZnSO_4$ and $ZnSO_4$-SPS (0.05 M, 0.1 M, 0.2 M) electrolytes before the electrochemical test.

Supplementary Note. 1 It is worth noting that the pH value of $ZnSO_4$ is turned from 3.85 to 3.89, 3.96 and 4.06 with the concentration of SPS increasing from 0.05 M, 0.1 M and 0.2 M, as shown in Fig. S1. The higher pH value suggests the introduction of SPS could reduce the amount of H^+ in the electrolyte and inhibit the HER.[3] In addition, it is far below 5.47 and will not continuously generate electrochemically inert $Zn_4SO_4(OH)_6 \cdot xH_2O$ (ZHS) at the interface to weaken the cyclic reversibility of the battery.[4]

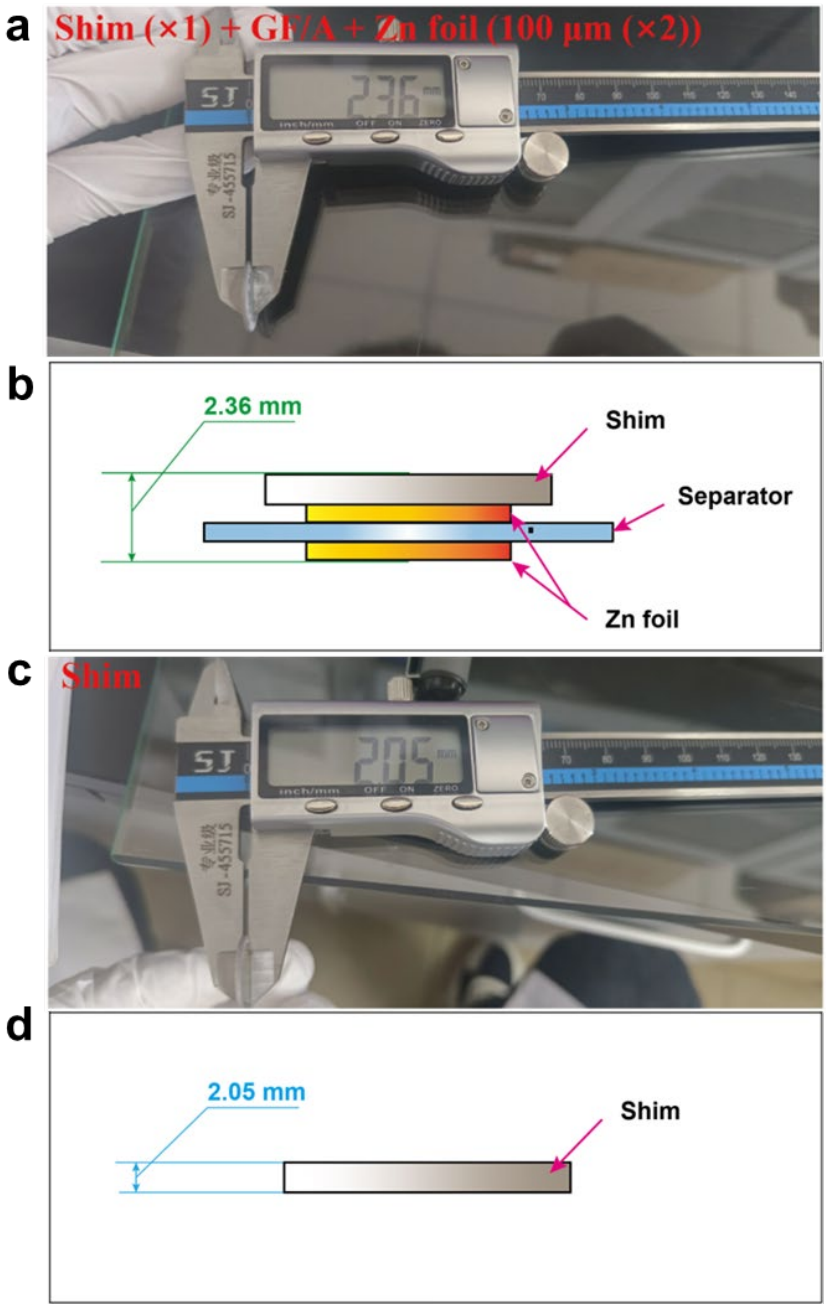


Figure S2. The measurement of the components of Zn/Zn cells to define the actual working thickness of GF/A separator. (a, b) The total thickness of the shim, zinc foil (100 μm) and GF/A separator. (c, d) The thickness of the shim.

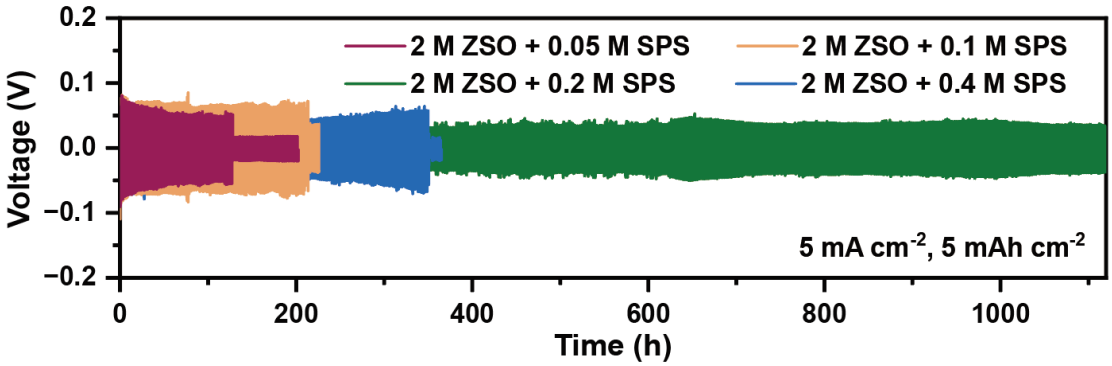


Figure S3. The cycling performance of different concentrations (0.05 M, 0.1 M, 0.2 M, 0.4 M) of the addition of SPS in 2 M $ZnSO_4$ at 5 mA cm^{-2}, 5 mAh cm^{-2}.

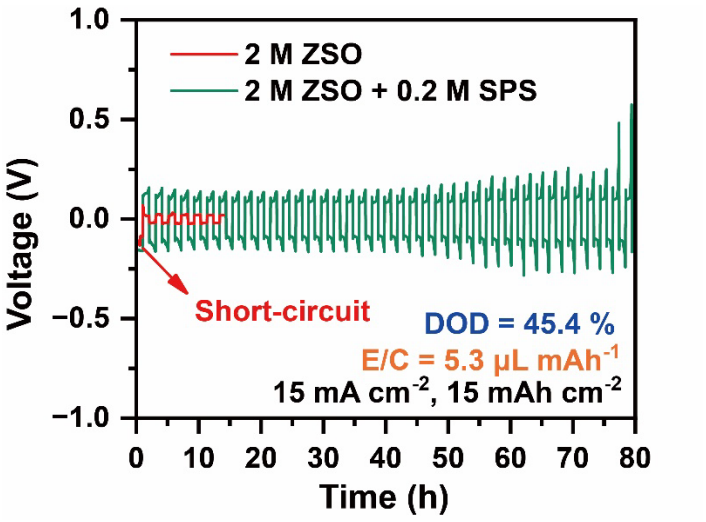


Figure S4. Galvanostatic cycling performance at 15 mA cm^{-2}, 15 mAh cm^{-2} under a high DOD (45.4%) condition (Zn foil Thickness: 50 μm).

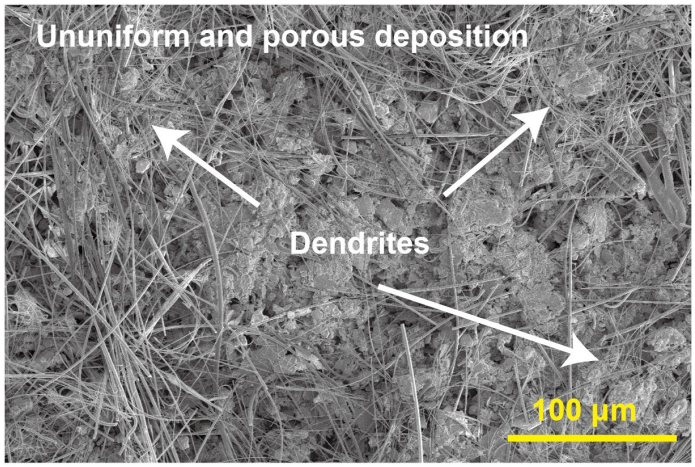


Figure S5. The SEM image of the Zn foil cycled in $ZnSO_4$ electrolyte during the rate test (Fig. 3f) which was a short circuit at 3 mA cm^{-2}.

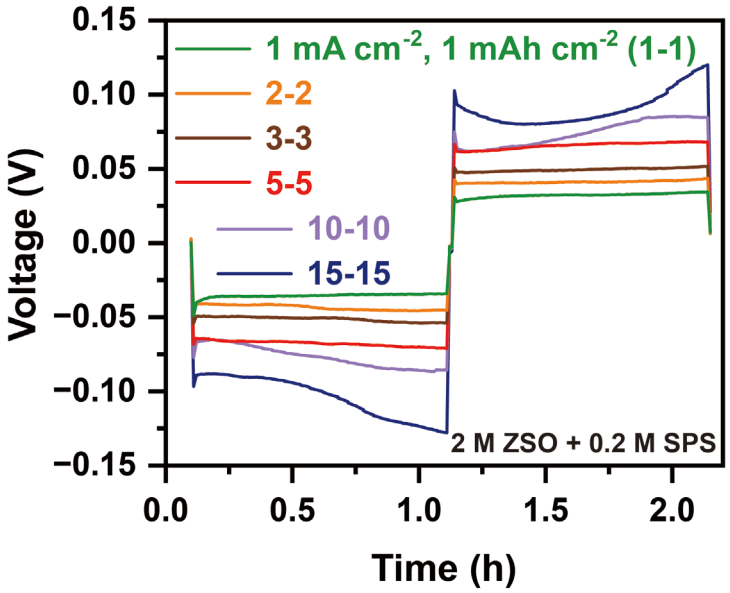


Figure S6. The stripping/depositing Voltage-Time curves at different current densities and capacities. (From 1 mA cm^{-2}, 1 mAh cm^{-2} to 15 mA cm^{-2}, 15 mAh cm^{-2}.)

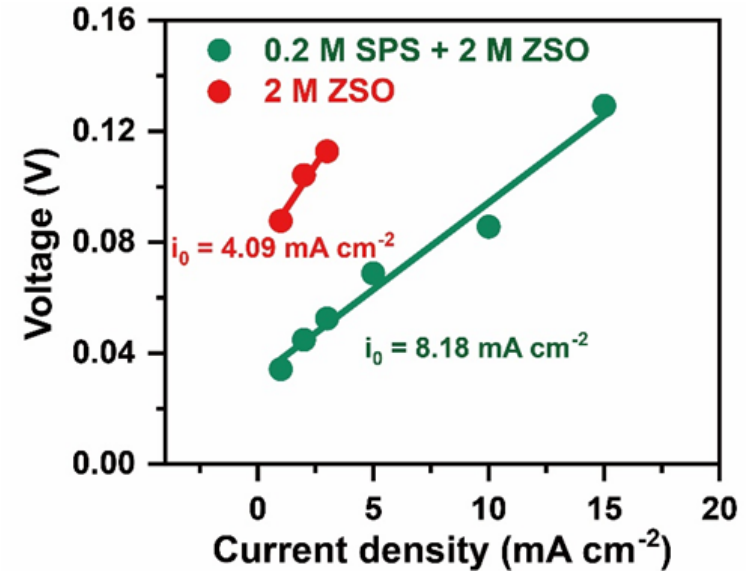


Figure S7. The exchange current density in $ZnSO_4$ and $ZnSO_4$-SPS electrolytes.

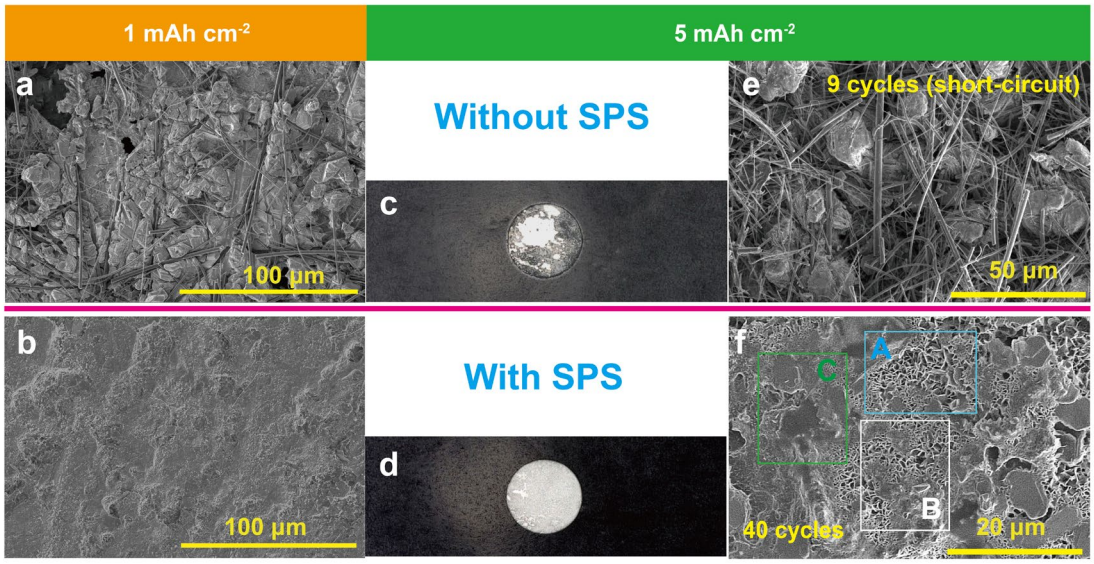


Figure S8. The characterization of the inhibition of dendrites with the addition of SPS. The morphologies of zinc foils cycled 75 times in (a) $ZnSO_4$ and (b) $ZnSO_4$-SPS electrolyte at 5 mA cm^{-2}, 1 mAh cm^{-2}. The overall deposited surface morphology of the cycled zinc foils after 9 times (short-circuit) in (c) $ZnSO_4$ and 40 times in (d) $ZnSO_4$-SPS system at 5 mA cm^{-2}, 5 mAh cm^{-2}. (e, f) SEM images of surface micro-morphologies of $ZnSO_4$ and $ZnSO_4$-SPS system related to Fig.S8c and Fig.S8d at 5 mA cm^{-2}, 5 mAh cm^{-2}, respectively.

Supplementary Note. 2 To investigate the inhibitory effect of SPS on dendrite formation, the cycled Zn anodes, cycled at various capacities, were subjected to SEM analysis. The SEM results of cycled zinc foil in $ZnSO_4$ electrolyte without and with SPS addition for 75 cycles at 5 mA cm^{-2}, 1 mAh cm^{-2} are shown in Fig. S8 (a, b), respectively. The surface morphology of cycled zinc foil in $ZnSO_4$ electrolyte was uneven, many dendrites and cavities were observed on the anode. This is due to the tip effect and the uneven charge distribution on the surface of the zinc foil. For the porous glass fibre separator, the uneven porous cavity morphology will aggravate the dendrite expansion and even puncture the separator and cause a short-circuit failure. On the contrary, the morphology of Zn foil cycled in $ZnSO_4$-SPS electrolyte appeared highly uniform, dense and flat, which reflects the strong homogenization of electric field and inhibition of dendrite growth due to SPS electrolyte additive. Fig. S8 (c, d) shows the cycled surface morphology of $ZnSO_4$ (9 cycles, short-circuit) and $ZnSO_4$-SPS (40 cycles) under 5 mA cm^{-2}, 5 mAh cm^{-2}, respectively. Many visible black dendrite particles can be observed after cycling in $ZnSO_4$ system. Additionally, the separator and deposition layer of Zn have grown together and cannot be separated which will lead to the stress on the glass fiber breaking the uniform structure of the separator. Furthermore, there is a clear difference between the regions of the galvanized area (dark) and the un-plated area (bright), suggesting the apparent uneven electroplating of Zn in $ZnSO_4$ which will provide conditions for the dendrite's growth. However, the electroplating layer of Zn in $ZnSO_4$-SPS was uniform, and no visible large dendrites were observed and the deposited Zn did not pierce the separator around the zinc foil. The related morphology of the SEM (Fig. S8e) shows the tip effect is exacerbated by high currents, and large-size dendrites (over 10 μm) grew on the Zn surface and penetrated the separator. However, in $ZnSO_4$-SPS in Fig. S8f, the surface of the cycled zinc foil is flat, and no separator fibres were found on the cycled Zn surface. The result in Fig. S8f shows the zinc deposited following vertical directions in $ZnSO_4$-SPS at high currents. There are a large number of high-index surfaces in area A, and with the continuous deposition of zinc, the inter-plane voids of high-index surfaces are gradually filled as shown in area B, and finally completely filled as shown in area C. The advantage of this gradual filling deposition mode is that the compactness of the deposited can be maximized. The thickness of the deposited Zn is reduced and the evenness of the deposition is improved. Compared to other loose deposition, Zn deposited with dense bulk morphology exhibits a lower electrolyte contact surface, resulting in minimal side reactions. In addition, the Zn consumption and the formation of "dead zinc" during cycling are low.[5]

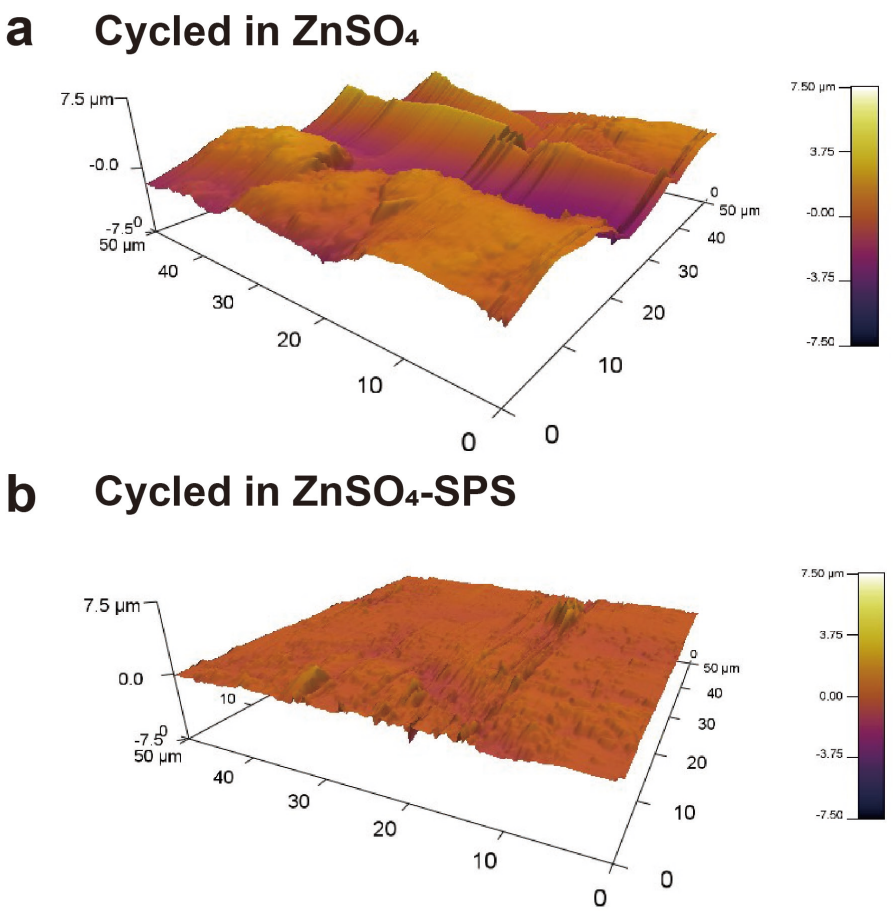


Figure S9. The AFM results of the zinc foils after 5 cycles in $ZnSO_4$ and $ZnSO_4$-0.2 M SPS at 2 mA cm^{-2}, respectively.

Supplementary Note. 3 To quantitatively explore the contribution of SPS to uniform deposition, AFM was used to characterize the surface roughness of zinc foil after cycling in Fig. S9. The results showed that the maximum height difference of zinc foil after cycling in $ZnSO_4$ was 7.9 μm, and the surface was significantly uneven. With the addition of SPS, the height difference was reduced to 3.3 μm and the uniformity of the deposition was improved.

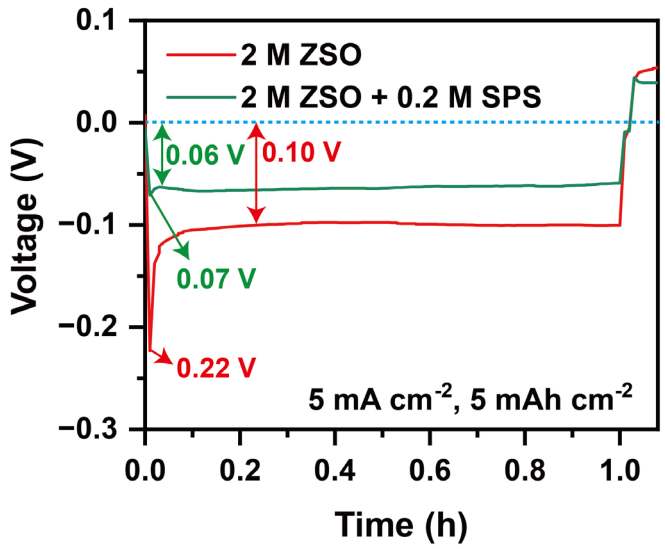


Figure S10. Potentials of Zn/Zn cells with and without SPS addition in the 1st cycle.

Supplementary Note. 4 The first-turn polarization voltage analysis of symmetrical cells was set to explore the stripping/plating mechanism of Zn in Fig. S10. The over-potential of the symmetrical cell in $ZnSO_4$ increases rapidly from 0 V to 0.22 V corresponding to the initial plating resistance, and then drops to a stable polarization voltage of 0.10 V. The high initial resistance represents the high energy barrier for the deposition of Zn.[5] As a comparison, the overpotential of the system in $ZnSO_4$-SPS system increases to only 0.07 V, which means that the SPS can reduce the energy barrier of the nucleation and deposition process of Zn on fresh Zn foil. Moreover, the stable polarization voltage is 0.06 V, suggesting that the addition of SPS can accelerate the subsequent plating process of Zn while ensuring the uniformity of plating as well.

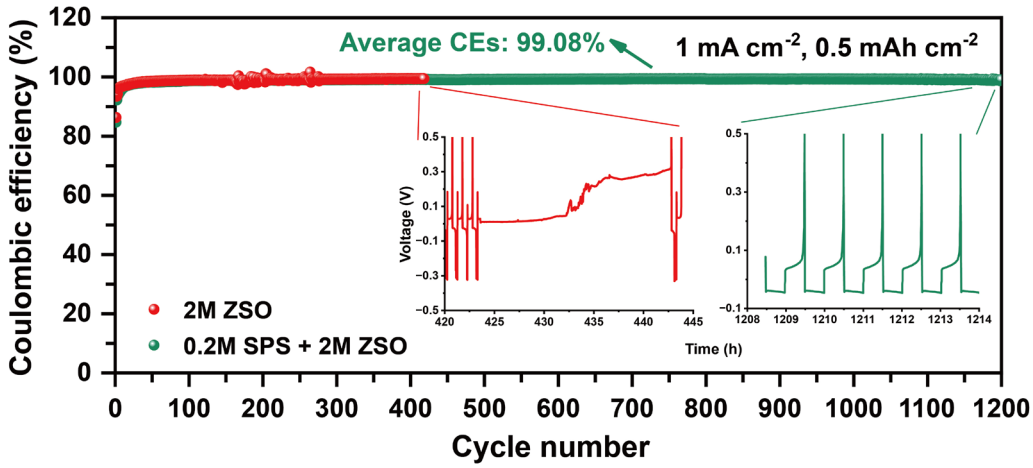


Figure S11. The cycling performance of Zn/Cu cells in $ZnSO_4$ and $ZnSO_4$-SPS electrolytes with a cut-off voltage of 0.5 V at 1 mA cm^{-2}, 0.5 mAh cm^{-2}.

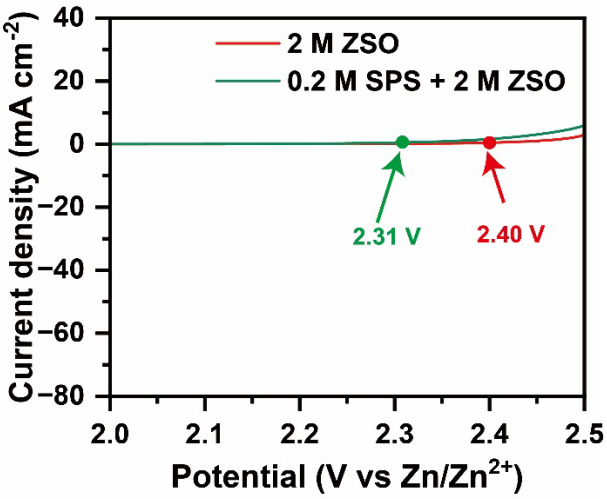


Figure S12. Linear sweep voltammetry (LSV) test for OER (Oxygen Evolution Reaction) with and without SPS at a scan rate of 5 mV/s.

Supplementary Note. 5 The results (Fig. S12) show that the OER inflection point of the $ZnSO_4$ system is 2.40 V, while that of the $ZnSO_4$-SPS system is 2.31 V. The addition of SPS will lead to a narrow OER window. However, the OER inflection point of 2.31V is still enough to match most of the aqueous zinc battery cathode materials.

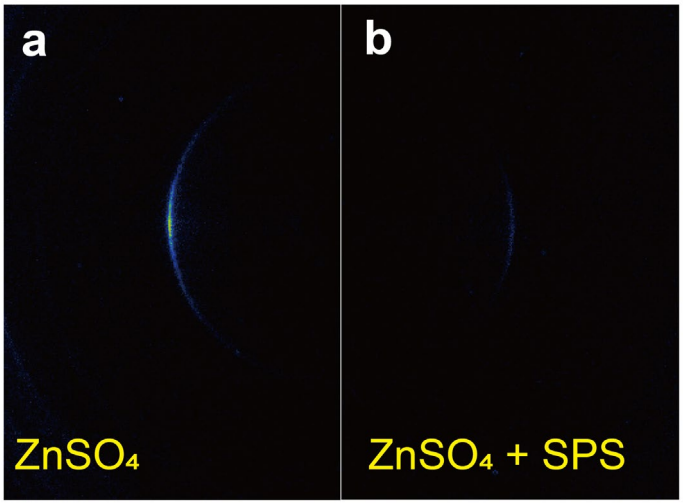


Figure S13. The GIWAXS results of the zinc foils cycled in 2 M $ZnSO_4$ and $ZnSO_4$-0.2 M SPS systems.

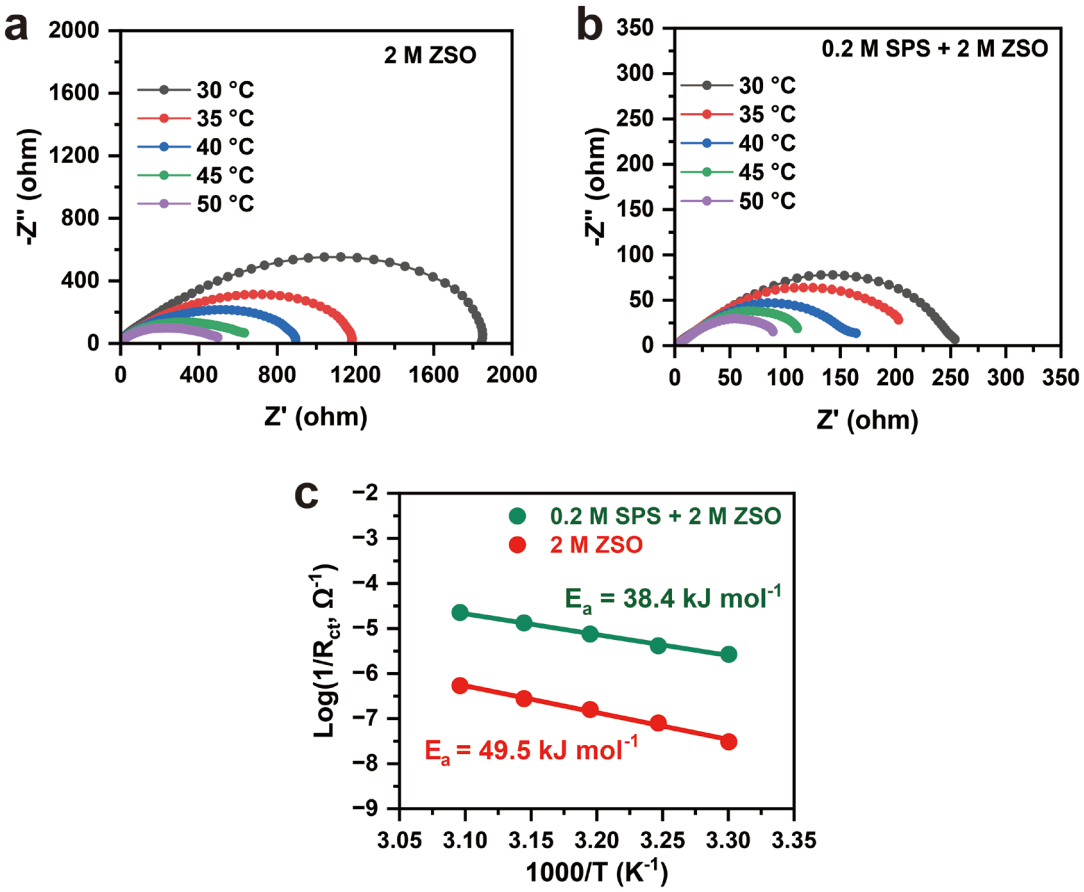


Figure S14. (a, b) EIS results at different temperatures from 30 °C to 50 °C of Zn/Zn cells in $ZnSO_4$ (the scale is from 0-2000 Ω) and $ZnSO_4$-SPS electrolytes (the scale is from 0-350 Ω) with a frequency range from 0.01 Hz to 100000 Hz (5 mV amplitude), respectively; (c) The calculated activation energy of $ZnSO_4$-SPS and $ZnSO_4$ systems.

Supplementary Note. 6 According to the Arrhenius equation shown below, the de-solvation activation energy was calculated.

$$1/R_{ct}=A\exp(-E_a/RT) \quad (1)$$

Where R is the gas constant, T is the temperature (K), R_{ct} is the interface transmission impedance, and E_a is the activation energy.

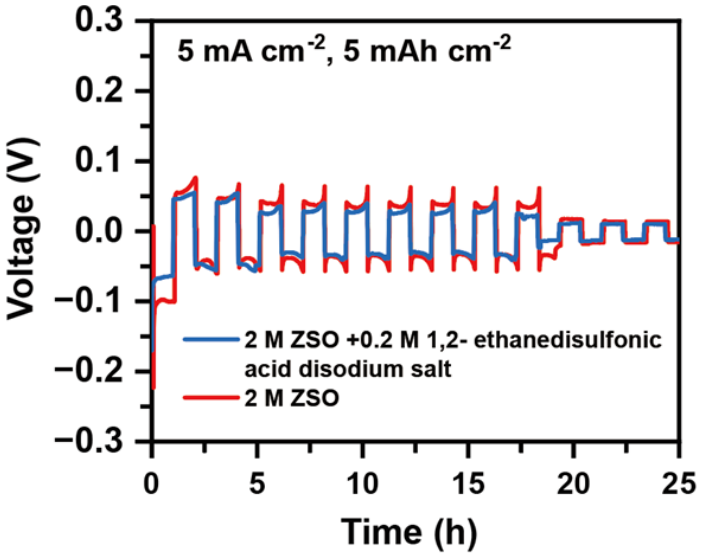


Figure S15. The cycling performance of the symmetrical cells in 2 M $ZnSO_4$ with and without the addition of 0.2 M 1,2-ethanedisulfonic acid disodium salt at 5 mA cm^{-2}, 5 mAh cm^{-2}.

Supplementary Note. 7 To further prove the main adsorbing function of -S-S-, 1,2-ethanedisulfonic acid disodium salt, which also contains two -SO_3 groups at the end of the chain similar to SPS, was tested with symmetrical batteries. The results, as shown in Fig. S15, indicate that the cycling life is not improved compared to the pure $ZnSO_4$ electrolyte and is much lower than that of SPS (1120 h) with the same addition (0.2 M) of 1,2-ethanedisulfonic acid disodium. However, the initial overpotential in $ZnSO_4$-1,2-ethanedisulfonic acid disodium system is 0.17 V which is lower than that in $ZnSO_4$ (0.22 V). In addition, the value and fluctuation of cycled overpotential in $ZnSO_4$-1,2-Ethanedisulfonic acid disodium system is also lower than those in $ZnSO_4$, demonstrating that -SO_3 groups could decrease the deposition energy barrier and Zn consumption from side reactions due to the desolvation effect. Through an evaluation comparing the cycling life of the addition of SPS and 1,2-Ethanedisulfonic acid disodium, the results indicate that the -S-S- group plays an important adsorption role in SPS to stabilize the adsorption layer. The MD results illustrate that -SO_3 plays a crucial role in the de-solvation of $[Zn(H_2O)_6]^{2+}$. It appears that the -S-S- and -SO_3 groups of SPS construct a dynamic guide layer that can provide plenty of nucleation sites for Zn deposition through uniform adsorption, thereby guiding zinc ion transport. In addition, the adsorbing layer can then isolate direct contact between water and the zinc anode and provide dynamic protection for the zinc anode to suppress side reactions.

In addition, through the test in Fig. S15, the effect of Na^+ on the dendrites was researched. The addition of 0.2 M 1,2-ethanedisulfonic acid disodium salt, which has the same concentration of Na^+ as 0.2 SPS in the electrolyte, could not prolong the cycling life of the cell demonstrating that the enhancement is mainly attributed to the organic chain in SPS.

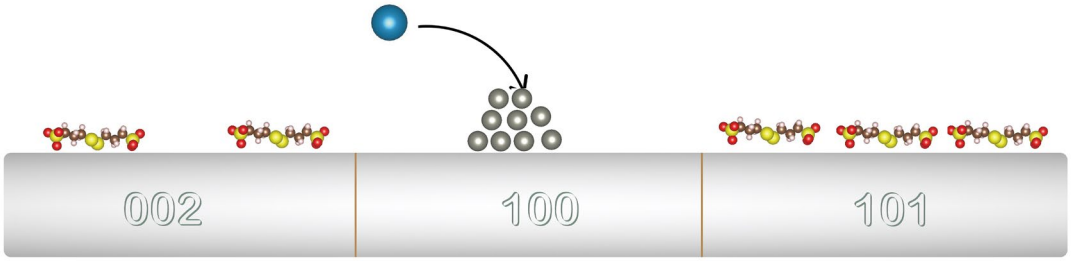


Figure S16. The schematic diagram of Zn deposition under a trace addition of SPS.

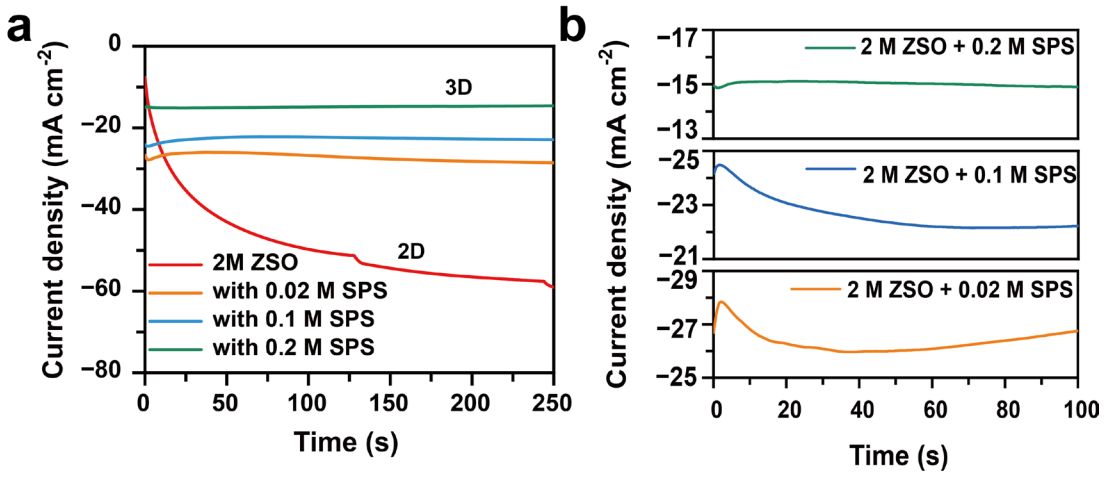


Figure S17. The CA tests of Zn/Zn cells in $ZnSO_4$ with the addition of 0.02, 0.1 and 0.2 M SPS at an overpotential of 150 mV, respectively.

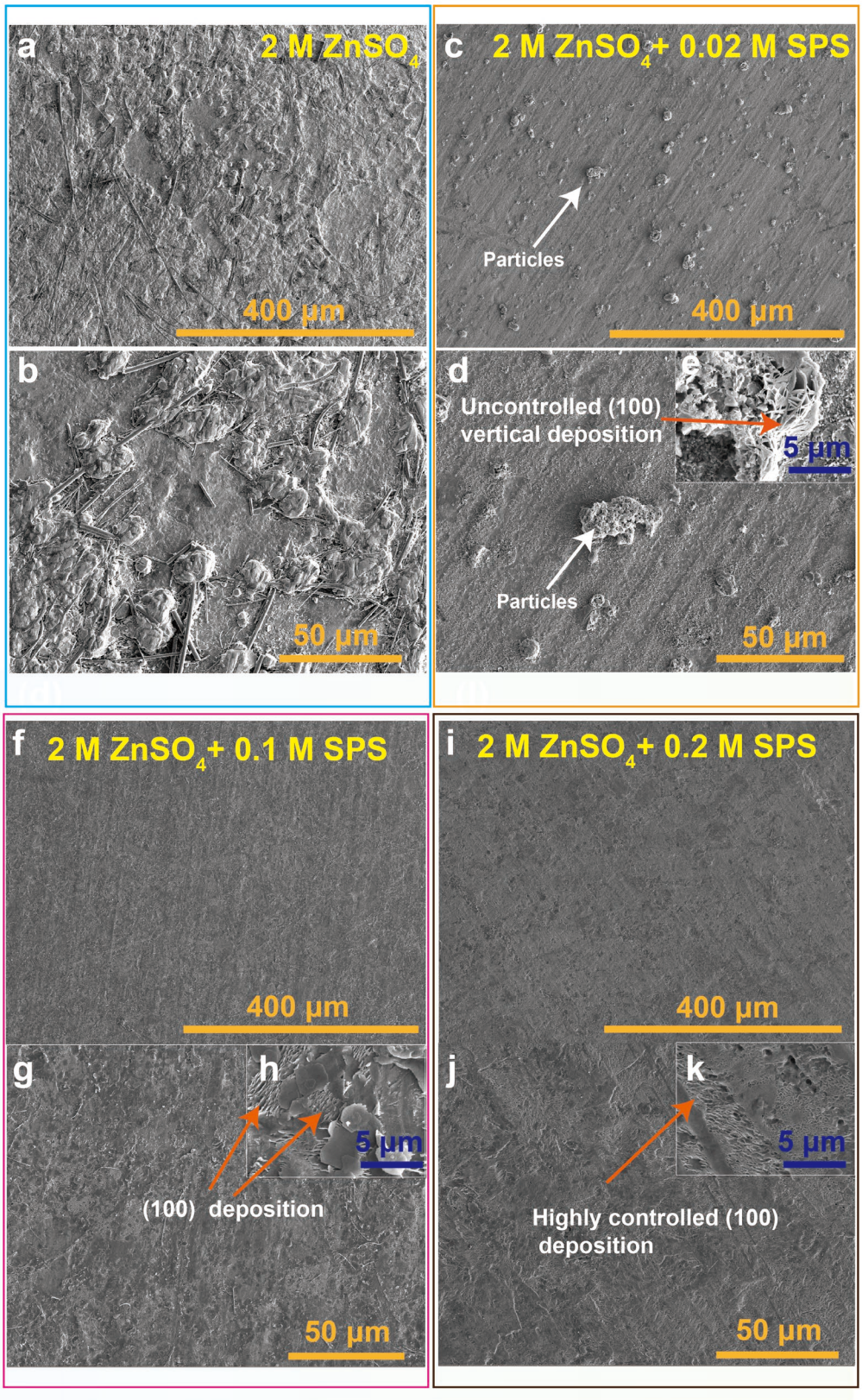


Figure S18. The SEM morphologies of the zinc foil cycled at an overpotential of 150 mV within 100 s in (a, b) $ZnSO_4$, (c-e) $ZnSO_4$-0.02 M SPS, (f-h) $ZnSO_4$-0.1 M SPS and (i-k) $ZnSO_4$-0.2 M SPS.

Supplementary Note. 8 Chronoamperometry (CA) was employed to further demonstrate the induction effect of SPS on (100) crystal planes in Fig. S17a. The results of $ZnSO_4$ exhibit a typical 2D diffusion behavior which is a random uncontrollable diffusion due to the tip effect.[6] The current of $ZnSO_4$-SPS is stable after 50 s, suggesting a controlled 3D diffusion. However, the CA curves fluctuated differently at various SPS concentrations, as shown in Fig. S17b. When the concentration of SPS is gradually increased from 0.02 M to 0.2 M, the fluctuation of the current with time gradually decreases, indicating that the diffusion and deposition of Zn^{2+} are strongly controlled with an increase in SPS concentration. To further explore the influence of the current fluctuation on the morphology of zinc deposition, zinc foils after 100 s of deposition were observed in Fig. S18. For the $ZnSO_4$ system, the random deposition and large dendrites (>10 μm) can be observed. Some large zinc particles also could be observed on the surface with a trace SPS addition of 0.02 M, which are loose and vertically growing high index crystals demonstrating an uncontrolled (100) deposition as illustrated in Fig. S16. In contrast, the 0.2 M SPS system is dense and flat with high index surface (100) deposition demonstrating a highly controlled electroplating process, which can effectively reduce the contact area with the electrolyte and inhibit the side reactions, as well as provide conditions for subsequent uniform deposition.

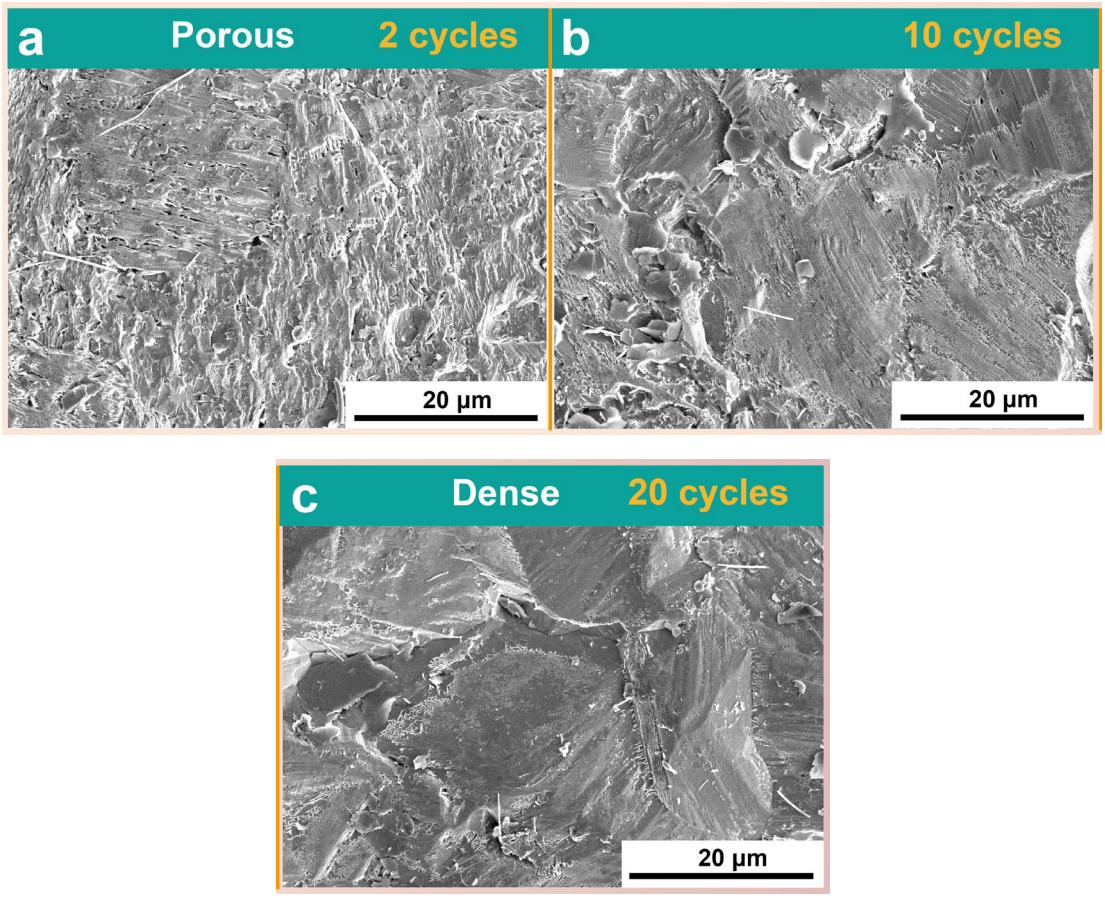


Figure S19. (a-c) SEM (secondary electron) images of the anode surface cycled 2, 10 and 20 times in $ZnSO_4$-SPS electrolyte, respectively.

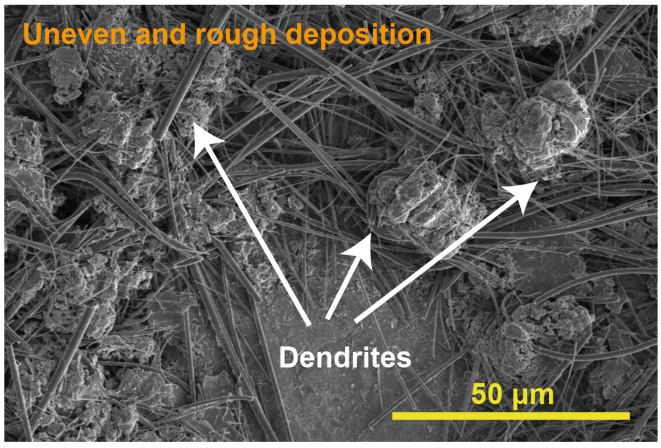


Figure S20. The SEM image of the Zn foil cycled 20 times in $ZnSO_4$ electrolyte. Compared with Fig. S19c, the obvious dendrites could be observed on the zinc anode surface after cycling demonstrating a random and non-uniform deposition in $ZnSO_4$ system.

Supplementary Note. 9 The SEM morphology as shown in Fig. S19, also gives strong proof of the high-index plane deposition mode. After two cycles, the surface of the zinc anode shows a flat morphology of vertical growth. However, there are small pores and gaps between different deposition sheets. After the 10th cycle, a relatively dense and flat deposit can be clearly observed. After 20 times of repeated stripping/depositing, the morphology of the Zn anode is extremely dense and no pores and crevices were observed. In contrast, the morphology of the cycled zinc foil (20 cycles, Fig. S20) in 2 M $ZnSO_4$ electrolyte is severely uneven and the deposition is rough. The large particles (over 20 μm) can be observed which formed by porous small sedimentation sheets. Porous, uneven deposits increase the thickness of a given mass of deposited layer and increase the contact area of Zn and water which tend to grow dendrites and provide conditions for the HER. The uniform and dense (100) deposition achieved by the addition of SPS can effectively inhibit the nucleation growth of dendrites. Additionally, due to the dense deposition, the contact area with the electrolyte can be effectively reduced, which is conducive to inhibiting HER and corrosion reactions and improving the cycle life and reversibility of the zinc anode.

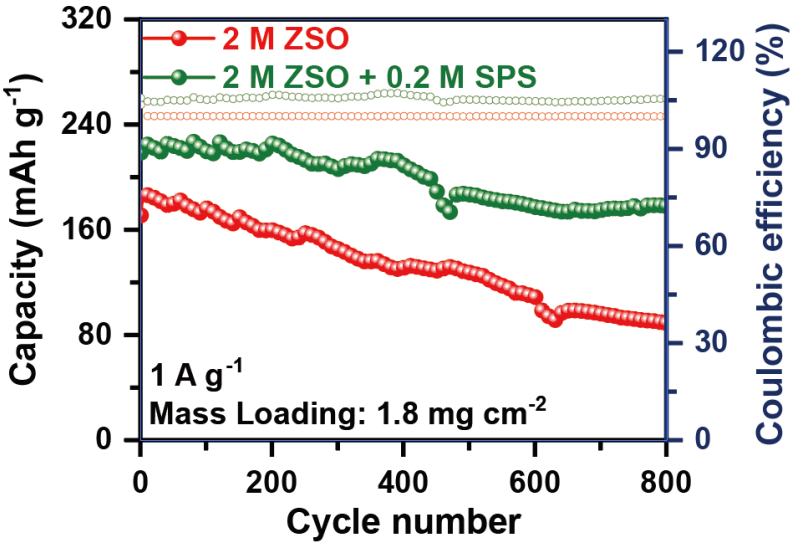


Figure S21. Long cycling tests for Zn/$NaV_3O_8 \cdot 1.35H_2O$ full batteries at 1 A g^{-1} with a mass loading of 1.8 mg cm^{-2}.

Supplementary Note. 10 At a current density of 1 A g^{-1}, a long-cycle test was performed as shown in Fig. S21. The result shows that $ZnSO_4$-SPS has a high initial capacity (219 mAh g^{-1}) relative to the $ZnSO_4$ battery (171 mAh g^{-1}). After 800 cycles, the specific discharge capacity of $ZnSO_4$-SPS is 178 mAh g^{-1} and the capacity retention rate is 81.3%, while the discharge specific capacity of $ZnSO_4$ is 89 mAh g^{-1} and the capacity retention rate is 52% after 800 cycles. The results show that the addition of SPS can enhance the cycling stability of the full cell. This is because SPS can inhibit the corrosion reaction on the surface of the zinc anode and avoid the generation of inert corrosion products, thereby improving the stability of the battery.

Table S1. Performance compared with other published works of Zn/Zn cells in $ZnSO_4$ electrolyte.

Additive	Added amount	Concentration of $ZnSO_4$	Current density (mA cm^{-2})	Areal capacity (mAh cm^{-2})	Lifespan (h)	Reference
SPS	0.2 M	2 M	5	5	1120	This work
SPS	0.2 M	2 M	1	1	2100	This work
TXA	50 mM	2 M	5	5	700	[7]
C_3N_4QDs	0.5 mg ml^{-1}	2 M	1	1	1200	[8]
TBA_2SO_4	0.05 mM	2 M	5	2	456	[9]
SMD	80 mM	2 M	5	3	1400	[10]
Na-L	40 mM	2 M	2	1	1500	[11]
SL	0.05 M	2 M	1	5	1000	[12]
EDTA-2Na	0.1 M	2 M	5	2.5	500	[13]
FEC	1 vol%	2 M	4	1	1000	[14]
TAU	1 M	2 M	5	5	500	[15]
DMSO	20 vol%	2 M	3	3	200	[16]
Suc	10 mM	1 M	2	2	500	[17]
CTAB	0.2 M	1 M	4	4	400	[18]
NHP	25 mM	1 M	5	5	315	[4]

Reference

[1] Z. Xie, J. Lai, X. Zhu, Y. Wang, *ACS Appl. Energy Mater.* **2018**, *1*, 6401-6408.

[2] A. Naveed, H. Ai, T. Li, A. Ali, J. M. Moradian, W. A. Qureshi, M. Su, X. Li, Y. Zhou, R. Guo, T. Wan, C.-H. Lin, D. Chu, Y. Liu, *Adv. Funct. Mater.* **2024**, *34*, 2400949.

[3] M. Liu, P. Wang, W. Zhang, H. He, G. He, S. Xu, L. Yao, T. S. Miller, *Energy Storage Mater.* **2024**, *67*, 103248.

[4] W. Zhang, Y. Dai, R. Chen, Z. Xu, J. Li, W. Zong, H. Li, Z. Li, Z. Zhang, J. Zhu, F. Guo, X. Gao, Z. Du, J. Chen, T. Wang, G. He, I. P. Parkin, *Angew. Chem. Int. Ed.* **2023**, *62*, e202212695.

[5] Q. Li, A. Chen, D. Wang, Y. Zhao, X. Wang, X. Jin, B. Xiong, C. Zhi, *Nat. Commun.* **2022**, *13*, 3699.

[6] Z. Li, W. Deng, C. Li, W. Wang, Z. Zhou, Y. Li, X. Yuan, J. Hu, M. Zhang, J. Zhu, W. Tang, X. Wang, R. Li, *J. Mater. Chem. A* **2020**, *8*, 17725-17731.

[7] J. Yin, H. Liu, P. Li, X. Feng, M. Wang, C. Huang, M. Li, Y. Su, B. Xiao, Y. Cheng, X. Xu, *Energy Storage Mater.* **2023**, *59*, 102800.

[8] W. Zhang, M. Dong, K. Jiang, D. Yang, X. Tan, S. Zhai, R. Feng, N. Chen, G. King, H. Zhang, H. Zeng, H. Li, M. Antonietti, Z. Li, *Nat. Commun.* **2022**, *13*, 5348.

[9] A. Bayaguud, X. Luo, Y. P. Fu, C. B. Zhu, *ACS Energy Lett.* **2020**, *5*, 3012-3020.

[10] S. Zheng, Y. Wang, B. Luo, L. Sun, G. Duan, J. Huang, Z. Ye, *Chem. Eng. J.* **2023**, *473*, 145313.

[11] Z. Hu, F. Zhang, A. Zhou, X. Hu, Q. Yan, Y. Liu, F. Arshad, Z. Li, R. Chen, F. Wu, L. Li, *Nano-Micro Lett.* **2023**, *15*, 171.

[12] H. Cao, X. Huang, Y. Li, Y. Liu, Q. Zheng, Y. Huo, R. Zhao, J. Zhao, D. Lin, *Chem. Eng. J.* **2023**, *455*, 140538.

[13] J. Cao, D. Zhang, R. Chanajaree, Y. Yue, Z. Zeng, X. Zhang, J. Qin, *Advanced Powder Materials* **2022**, *1*, 100007.

[14] D. Xie, Y. Sang, D.-H. Wang, W.-Y. Diao, F.-Y. Tao, C. Liu, J.-W. Wang, H.-Z. Sun, J.-P. Zhang, X.-L. Wu, *Angew. Chem. Int. Ed.* **2023**, *62*, e202216934.

[15] X. Xu, J. Yin, R. Qin, H. Liu, X. Feng, M. Wang, M. Li, W. Sun, W. Shi, B. Xiao, Y.

Su, Y. Cheng, *J. Energy Chem.* **2023**, *86*, 343-350.

[16] D. Feng, F. Cao, L. Hou, T. Li, Y. Jiao, P. Wu, *Small* **2021**, *17*, 2103195.

[17] C. Wang, J. Hou, Y. Gan, L. Xie, Y. He, Q. Hu, S. Liu, S. Chan Jun, *J. Mater. Chem. A* **2023**, *11*, 8057-8065.

[18] Z. Liu, R. Wang, Y. Gao, S. Zhang, J. Wan, J. Mao, L. Zhang, H. Li, J. Hao, G. Li, L. Zhang, C. Zhang, *Adv. Funct. Mater.* **2023**, *33*, 2308463.



https://dspace.org/

Engineering aqueous electrolytes with vicinal sbased organic additives for highly reversible zincion batteries

Li, Teng; Naveed, Ahmad; Zheng, Jiongzhi; Chen, Bixian; Jiang, Mingfeng ...

2025-05-19
Wiley
https://doi.org/10.1002/ange.202424095
Li T, Naveed A, Zheng J, et al., (2025) Engineering aqueous electrolytes with vicinal sbased organic additives for highly reversible zincion batteries. Angewandte Chemie, Volume 137, Issue 21, May 2025. Article number e202424095

Downloaded from a DSpace repository. https://dspace.org/